

PREPARED FOR SUBMISSION TO JINST

A terahertz pump mega-electron-volt ultrafast electron diffraction probe apparatus at SLAC Accelerator Structure Test Area facility

B. K. Ofori-Okai,^{a,b} M. C. Hoffmann,^a A. H. Reid,^a S. Edstrom,^a R. K. Jobe,^a R. Li,^a E. M. Mannebach,^{c,d} S. J. Park,^{a,c} W. Polzin,^a X. Shen,^a S. P. Weathersby,^a J. Yang,^a Q. Zheng,^a M. Zajac,^{a,c} A. M. Lindenberg,^{c,d,e} S. H. Glenzer,^a X. J. Wang,^a

^a*SLAC National Accelerator Lab, 2575 Sand Hill Road, Menlo Park, CA 94025, USA*

^b*Department of Chemistry, Massachusetts Institute of Technology, 77 Massachusetts Avenue, Cambridge, MA 02139, USA*

^c*Stanford Institute for Materials and Energy Sciences, SLAC National Accelerator Laboratory, Menlo Park, CA 94025, USA*

^d*Department of Materials Science and Engineering, Stanford University, Stanford, California 94305, USA*

^e*PULSE Institute, SLAC National Accelerator Laboratory, Menlo Park, CA 94025, USA*

E-mail: benofori@SLAC.stanford.edu

ABSTRACT: We describe a new experimental setup capable of measuring structural dynamics following intense terahertz excitation. This system, developed at the SLAC Accelerator Structure Test Area facility, uses a high-energy ultrafast laser to produce intense terahertz pulses and femtosecond electron bunches that are accelerated to mega-electron-volt kinetic energies. The focused terahertz pulses have electric fields in excess of 600 kV/cm, and the resulting structural dynamics can be followed by electron diffraction. We also present some examples demonstrating its implementation where interactions between the THz pulses and the electron bunch are used to characterize the spatial and temporal characteristics of the THz field.

KEYWORDS: Accelerator applications, Optics, Imaging spectroscopy

Contents

1	Introduction	1
2	Apparatus design and implementation	2
3	Pumping capabilities	4
4	Applications	6
4.1	Spatial Characterization	6
4.2	Temporal Characterization	7
5	Conclusions and outlook	9

1 Introduction

One of the main challenges of ultrafast time-resolved optical spectroscopy is to correctly determine which microscopic quantity, such as electron density or atomic structure, is responsible for observed changes in an optical quantity, such as reflectivity. Typically, inferences on the microscopic agents (free-carrier density, quasiparticles, lattice distortions) are made by analyzing the discernable time scale or oscillation period of the quantity being measured. Only with the recent developments of ultrafast short wavelength ($\lambda < 1 \text{ \AA}$) coherent radiation sources has it become possible to directly probe the structural dynamics following photoexcitation [1] or intense laser heating [2, 3]. Using either hard X-ray free-electron lasers (XFELs)[4, 5] or ultrabright electron bunches [6, 7], it is now possible to perform time-resolved diffraction with sub-ps resolution. Of these two, ultrafast electron diffraction (UED) benefits from the larger scattering cross-section of electrons compared to hard X-rays, making it more appropriate for studying thin samples and low-dimensional materials [8]. While X-rays scatter primarily off the electron density, electrons scatter off the atomic potential, making them more sensitive to atomic positions and light (low Z) elements. Electrons also produce less radiation damage per scattering event compared to X-rays [9]. As charged particles they can be easily manipulated by magnetic lenses for steering and focusing. With state-of-the-art radio frequency (rf) photoinjectors, electrons with mega-electron-volt (MeV) kinetic energies can be produced [10]. At these kinetic energies the electrons become relativistic, and effects of special relativity are able to mitigate the space charge force, $F_{sc} \propto 1/\beta^2\gamma^3$, which leads to temporal and transverse broadening. As a result, the bunch can remain temporally short and may be tightly focused [11] without reducing the bunch charge [1]. The short de Broglie wavelength of relativistic electrons allows for a large region of reciprocal space (q -space) to be measured simultaneously.

In order to take full advantage of ultrafast structural probes, it is necessary to combine them with different excitation sources. Most time-resolved UED measurements have used near-infrared (NIR) or visible wavelength pulses for photoexcitation. Compared to these, terahertz (THz) frequency

pulses offer a unique opportunity for perturbing the structures of materials. Intense THz pulses can resonantly drive low frequency ionic displacements, and can also change material properties through non-resonant interactions, similar to optical excitation, without significantly perturbing the electronic density of states [12–15]. The relatively long timescale (\sim ps) and low photon energies (\sim meV) of THz pulses make them well suited to interact more directly with the heavier ions that make up the lattice through dipole-active optic phonons. In addition, the excitations of many quasiparticles responsible for unique emergent behavior (e.g. excitons, magnons) occur on THz energy scales. Consequently, there is increasing interest in following the structural distortions of materials following intense THz excitation.

There have also been efforts in using intense THz pulses produced by optical means to manipulate electron bunches. It has been demonstrated that single-cycle THz pulses with fields exceeding 1 MV/cm could be used to accelerate electrons from rest to kinetic energies of 0.8 keV in a compact electron gun [16, 17]. THz acceleration of photoelectrons produced in noble gas jets has been used to develop X-ray streak cameras which provide accurate timing of free-electron lasers at FLASH, SACLA, and LCLS [18–21]. THz pulses have also been used to temporally compress and characterize bunches containing \sim 1000 electrons with kinetic energies of less than 100 keV to durations less than 100 fs [22]. A THz assisted electron diffraction scheme has been suggested for measuring ultrafast electron diffraction on molecules in the gas phase with sub-10 fs temporal resolution [23]. These applications further motivate understanding the interactions between THz pulses and ultrafast MeV electron bunches.

In this paper, we present the details of a newly developed instrument at the SLAC Accelerator Structure Test Area facility capable of investigating these phenomena. The system builds on the recently commissioned MeV-UED apparatus [24]. By utilizing an upgraded titanium sapphire femtosecond laser system, which delivers more than 28 mJ of uncompressed (\sim 120 ps) pulses, the new system has sufficient energy for generating intense THz fields for pumping samples as well as femtosecond electron bunches to probe the structural dynamics. The THz pulses are produced by optical rectification using either lithium niobate (LiNbO_3 , LN) [25–29], or the organic crystal 4-N,N-dimethylamino-4'-N'-methyl-stilbazolium 2,4,6-trimethylbenzenesulfonate (DSTMS) [30, 31] as the nonlinear medium. The spectrum of the resulting THz pulses has frequency content up to 5 THz, and when focused the peak field strength exceeds 600 kV/cm. In addition, the system possesses the ability for intense optical pumping at either 800 nm or 400 nm derived from the fundamental or second harmonic of the titanium sapphire laser, respectively, thereby enabling optical-THz double-pump experiments.

2 Apparatus design and implementation

Figure 1 shows a schematic of the new experimental system. Compared to the previous instrument [3, 11, 24], the apparatus possesses an upgraded laser system, new sample chamber, and optics for producing and detecting intense THz pulses.

The new laser system consists of a Coherent Legend Ti:sapphire regenerative amplifier, the output of which is passed into a second-stage multipass amplifier. This results in the production of uncompressed 800 nm pulses with pulse energies, E_p , exceeding 28 mJ and a stability (defined as the standard deviation of the pulse energy divided by the mean of the pulse energy) of $< 0.2\%$.

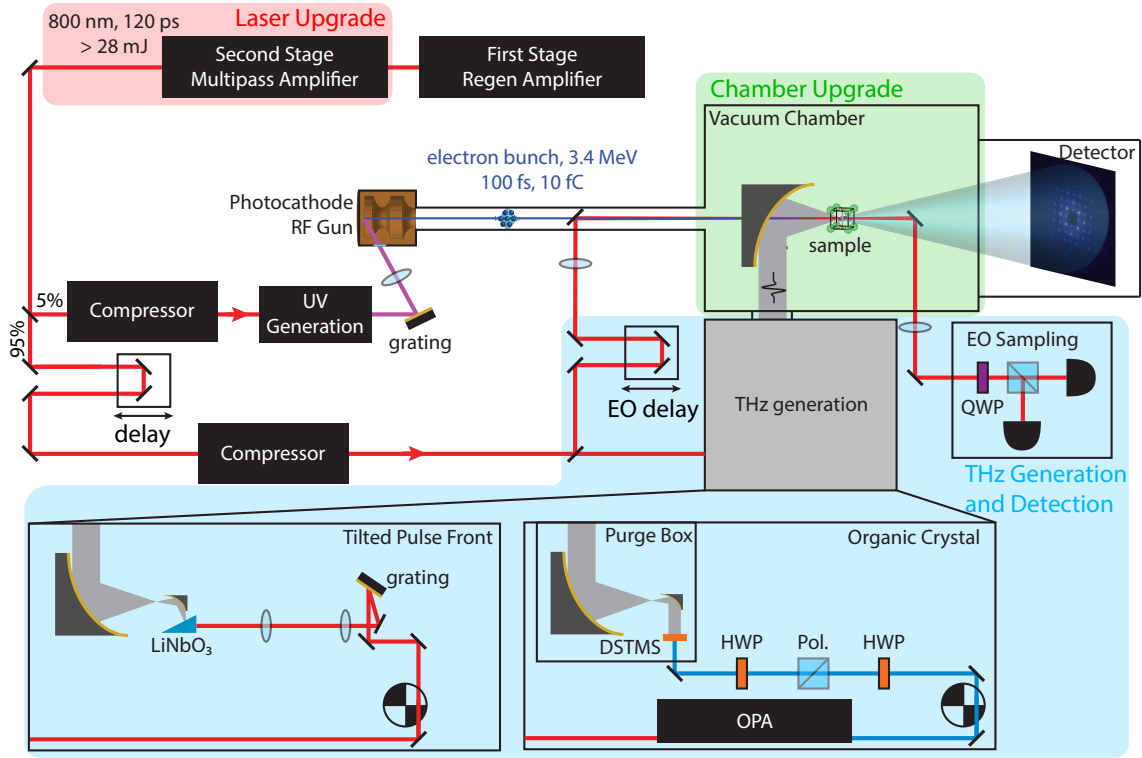


Figure 1. Schematic of optical setup highlighting the upgraded areas and new capabilities. The output of the new multi-pass amplifier is split and used to produce UV pulses by third harmonic generation as well as optical lines for THz generation by optical rectification and THz readout by electro-optic sampling. UV pulses are used to create femtosecond electron bunches that are accelerated to MeV kinetic energies. THz pulses are generated in an MgO-doped LN crystal using NIR pulses with tilted pulse fronts, or in DSTMS using 1350 nm light produced by a high power OPA.

The pulse bandwidth can be adjusted from 10 nm FWHM to almost 30 nm FWHM, which can yield pulses with a transform limited duration between 100 and 50 fs, respectively. Using a series of Pockels cells, the laser can be set to run in either single-shot mode or at a repetition rate of up to 180 Hz.

Following amplification, the uncompressed output is split by a beamsplitter, with greater than 95% of the energy directed into a mechanical delay stage and subsequently used for THz generation and characterization, as described in the next section. The remaining pulse energy is compressed by a single-grating compressor before being tripled using a pair of β -barium borate (BBO) crystals to produce $\lambda = 266$ nm UV pulses. These pulses are then diffracted off a grating before being imaged with a 1/8 demagnification onto the photocathode. The combination of imaging and diffraction by the grating is used to produce a tilted intensity front [32, 33] that compensates for the off-normal incidence angle of the beam ($\theta_i \sim 70^\circ$). Consequently, all spatial portions of the UV pulse simultaneously release photoelectrons, and this minimizes the bunch length.

The resulting photoelectrons are accelerated by a 1.6 cell photocathode rf gun, identical to one used at the SLAC Linac Coherent Light Source (LCLS) injector. The rf gun is powered by

a pulse-forming-network-based modulator and a 50-megawatt S-band klystron operating at 2.856 GHz. Both the phase and amplitude of the rf signal are monitored within the gun and are stabilized by a feedback loop. Typical values of the rf amplitude and phase stability of the gun fields were measured to be 3×10^{-4} (rms) and 30 fs (rms).

The relativistic kinetic energy, E_k , is tunable between 2.2 and 4 MeV. The corresponding Lorentz factor γ ranges from 4.9 to 8.8, and the de Broglie wavelength of the electrons, λ_e , given by,

$$\lambda_e = \frac{hc_0}{\sqrt{E_k^2 + 2E_k m_0 c_0^2}}, \quad (2.1)$$

varies from 0.51 pm to 0.28 pm, where $h = 6.626 \times 10^{-34}$ J s is Planck's constant, $c_0 = 3 \times 10^8$ m/s is the vacuum speed of light, and $m_0 = 9.11 \times 10^{-31}$ kg is the electron rest mass. The accelerated electrons travel through a drift tube to the sample chamber. The position and size of the electron beam at the sample position are controlled using two pairs of steering magnets and a focusing solenoid, respectively. The typical diameter of the electron beam at the sample position is 100 μm , but can be focused to less than 5 μm 1/e radius [11].

The sample card is mounted to an assembly capable of translating the sample along the x -, y -, and z -axes. The linear stages have maximum travel range of 25.4 mm and a reproducibility of < 5 μm . Rotation of the sample around the vertical (yaw) and horizontal (pitch) axes are also possible, with maximum rotation angles of $\pm 15^\circ$ each. The sample card is also connected to a compressed helium closed-loop cryogenic cooler which is capable of cooling the samples to below 40 K.

After interacting with the sample, the electrons travel through a 3.1 meter drift tube where the diffracted electrons are deposited onto a P43 phosphor screen. The undiffracted electrons pass through an $r = 1.3$ mm hole at the center of the phosphor screen. This phosphor screen is then imaged using an $f = 40$ mm focal length lens onto an electron multiplying charge-coupled device (EMCCD) camera (Andor iXon Ultra 888, 1024×1024 pixel, 26 max fps, 13 μm pixel size) with a demagnification of $M = 1/3$.

3 Pumping capabilities

The remaining $\sim 95\%$ of the laser energy is used for THz generation and characterization. The pulses are compressed and split into separate optical lines used for THz generation, by optical rectification (OR), and characterization, by electro-optic (EO) sampling. THz pulses are generated in either a MgO-doped stoichiometric LN crystal using tilted optical pulse fronts [28], or the organic crystal DSTMS [30]. For LN generation, pulses with energy of up to 15 mJ are used directly. For DSTMS, the 800 nm pulses pump a Light Conversion HE-TOPAS optical parametric amplifier (OPA) which produces 2 mJ pulses of 1350 nm light that are used for OR. In both cases, the fluence can be adjusted using a computer controlled waveplate and static polarizer to attenuate either the 800 nm or the 1350 nm pulses. In the DSTMS generation, the THz polarization can also be adjusted by rotating the polarization of the 1350 nm pulse as well as the DSTMS crystal. Additionally, the path of the THz pulse between the crystal and the chamber is enclosed by a dry-air purge box to minimize atmospheric water absorption.

The resulting THz pulses are collected and focused by a 25.4 mm diameter, 50.8 mm effective focal length off-axis parabolic reflector (OAP). This focused spot is relay imaged using a pair of OAPs onto the sample. This three mirror scheme allows for tighter focusing of the THz pulse, which increases the peak field strength [34]. The THz pulses are coupled into the sample chamber through a 3 mm Zeonex window located between the second and third OAPs. The final OAP is located in the sample chamber, has an effective focal length of 76.2 mm, and is motorized along the x -, y -, and z - axes for precise positioning of the THz beam. A hole drilled through the parabola allows overlap of the electron bunch or the EO sampling pulse with the THz pulse.

The EO sampling pulse is directed through a second mechanical delay stage before being focused using an $f = 500$ mm lens to the sample. The EO sampling beam is overlapped with the electron beam using a mirror with a 2 mm hole located at the center. The energy of the EO sampling pulse is controlled using a computer controlled half-waveplate and polarizer. In order to measure the pulse, a motorized mirror which can be moved into and out of the beam path is used to outcouple the EO sampling beam. A pair of balanced photodiodes and a lock-in amplifier were used to measure the THz time-domain waveform.

Figure 2(a) shows EO sampling data for the two different THz generation methods. Mimicking typical experimental conditions, these traces were measured using a $50\ \mu\text{m}$ thick $\langle 110 \rangle$ gallium phosphide (GaP) crystal mounted on the sample card in the chamber under vacuum. For both LN and DSTMS, the peak electric field exceeds $600\ \text{kV/cm}$. Figure 2(b) gives the spectrum obtained by Fourier transform of the time-domain waveforms. Artifacts caused by the reflections of the THz pulse in the thin GaP crystal were suppressed by Fourier transforming only a ± 1 ps window around the main cycle of the THz pulse. As reported previously, the spectrum of THz pulses produced by LN are at lower frequencies compared to those produced in DSTMS. We find the average frequency, $\langle \nu \rangle$, of 0.95 and 2.5 THz for LN and DSTMS sources, respectively, and the full width half maximum of the spectra, $\Delta \nu$, were 1.1 and 2.7 THz. The measured spot size of the pulse is 1.5 mm for the LN source, and 0.3 mm for the DSTMS source.

In this configuration, it is also possible to use the EO sampling beam to pump samples with either fundamental $800\ \text{nm}$, or second harmonic $400\ \text{nm}$ pulses. The full set of experimental capabilities available in the system is shown in table 1. For NIR or visible pumping, the optical beam can be focused to $r \sim 150\ \mu\text{m}$ without significant distortions to the beam shape from the hole in the mirror. By using the delay stage in the EO sampling beam line, the arrival time of both the NIR/visible pulse and the THz pulse can be set relative to the electron bunch, thereby enabling

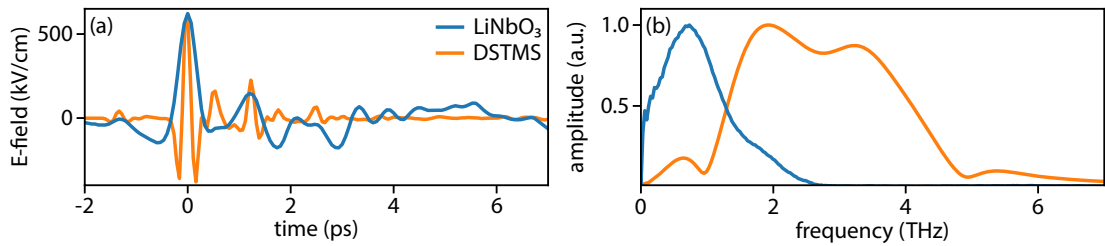


Figure 2. Comparison of THz sources in the (a) time- and (b) frequency-domain. A $50\ \mu\text{m}$ thick GaP crystal was used for EO sampling. The spectra were obtained using a ± 1 ps window around the main cycle of the THz pulse to avoid artifacts from etalon reflections in the thin EO crystal.

double-pump experiments.

Table 1. Experimental pumping capabilities available.

Source	Max E -field (kV/cm)	Max Pulse Energy	ν_0 (THz)	$\Delta\nu$ (THz)	FWHM Duration
LiNbO ₃	> 600	6 μ J	0.95	1.1	1 ps
DSTMS	> 600	2 μ J	2.56	2.7	0.3 ps
800 nm	–	300 μ J	–	–	<0.1 ps
400 nm	–	100 μ J	–	–	<0.1 ps

4 Applications

In order to demonstrate some of the features of the apparatus, we present a series of measurements in which we use the electron beam to characterize the THz field near the focus of the parabolic reflector. The measurements were performed using a pinhole with a radius of $r = 50 \mu\text{m}$ placed at the THz focal plane. The pinhole served to amplify the interactions between the THz fields and the electron beam by allowing momentum transfer. The pinhole is not expected to show a polarization dependent response due to the circular symmetry, unlike a slit or an antenna [35]. Thus, it is an ideal choice for unbiased characterization of the local THz field. For the examples described here, the THz pulses were produced using the DSTMS crystal, and the peak field strength was $\sim 550 \text{ kV/cm}$ as measured by EO sampling. For visualization purposes, the electron beam was steered away from the hole in the phosphor screen using the steering magnets downstream of the sample chamber.

The interaction of the THz pulse with the electron bunch resulted in a deflection of the electron beam due to the Lorentz Force law, $F = -e\vec{E}_{THz} + \vec{v} \times \vec{B}_{THz}$. In vacuum it is expected that the contributions from the electric and magnetic fields should cancel and hence there should be no force on the electron bunch. However, the pinhole preferentially enhances the electric field[36], and the cumulative effect of the enhanced field results in a transverse momentum kick, Δp . Though the magnitude of the integrated momentum kick depends on several factors (e.g. the dimensions of the pinhole, the spatial and temporal behavior of the THz pulse, the temporal walk-off between the electron bunch and the THz pulse through the pinhole), the deflection is essentially linear in the applied THz field [22]. Furthermore, as the direction is opposite to the sign of the incident field, this provides a means of determining the absolute direction and magnitude of the THz electric field.

4.1 Spatial Characterization

Figure 3 shows images of the electron beam at the detector in the absence (figure 3(a)) and presence (figure 3(b)) of the THz pulse. For these measurements, the bunch charge was increased so that the temporal duration of the bunch was longer than the 400 fs temporal period of the THz pulse, and the long exposure time of the camera averaged many shots into a single image. As a result, the interaction between the THz pulse and the electron bunch appears to streak the bunch along the vertical axis. The streaking can be characterized by the centroid-to-centroid distance as indicated in figure 3(b).

To characterize the spatial distribution of the THz field, streaking patterns were measured at a variety of positions around the THz focus. Each time, the pinhole was used to guide the

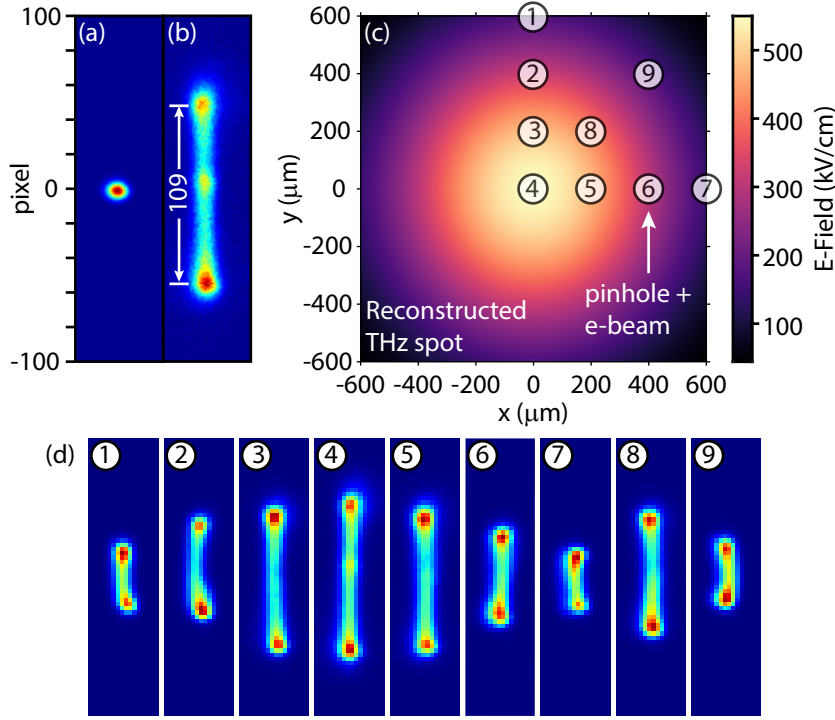


Figure 3. Image of electron beam at the phosphor screen in the (a) absence and (b) presence of the THz pulse. (c) Image of THz focus reconstructed from streaking measurements. (d) Streaking patterns recorded with pinhole at locations indicated 1-9.

electron beam to a different position in the THz focal plane, and the centroid-to-centroid values were measured at each location. The streaking values were fit to a two-dimensional Gaussian of the form $\exp(-x^2/\sigma_x^2 - y^2/\sigma_y^2)$, and this was used to construct a map of the THz field at the focus. The 2D fit had an R^2 value of 0.97, and the $1/e$ radii were $\sigma_x = 520 \mu\text{m}$ and $\sigma_y = 550 \mu\text{m}$. These are $5\times$ the limit expected for a Gaussian beam with $\lambda = 150 \mu\text{m}$. The reconstructed THz spot is shown in figure 3(c), with streaking patterns obtained at selected locations shown in figure 3(d). For locations far from the center of the focus, the streaking is not solely along the vertical direction indicating that there are some perpendicular component to the THz polarization. These components cannot be visualized directly by a conventional THz camera which is sensitive to the local *intensity* of the THz pulse rather than the local *field*.

4.2 Temporal Characterization

Lastly, we characterized the temporal dependence of the momentum kick. For this measurement the bunch charge was reduced so that the bunch duration was subcycle compared to the THz pulse, and the camera was set to record images of individual bunches. The time-delay between the THz pulse and the electron bunch was varied, and at each delay 50 images were recorded. The centroid position was obtained from each image and averaged to obtain the mean change in the centroid,

$\langle \Delta x_i \rangle$. This can be related to the average momentum kick experienced by the electron beam by,

$$\langle \Delta p_i \rangle = p_0 \frac{\langle \Delta x_i \rangle}{L}, \quad (4.1)$$

where $p_0 = \gamma \beta m_0 c_0$ is the incident longitudinal momentum and $L = 3.1$ m is the distance from the pinhole to the phosphor screen.

Figures 4(a) and 4(b) show three-dimensional plots of the transverse momentum kick along the x - and y - axes as a function of time delay for THz pulses polarized vertically and at $\sim 45^\circ$, respectively. The electron kinetic energy was set to 3.1 MeV, corresponding to a momentum $p_0 = 3.6$ MeV/c. As expected, for the vertically polarized field, the streaking is almost entirely along the vertical axis. In the case where the polarization is rotated, we observe a weakening of the vertical deflection as well as an additional horizontal deflection.

The maximum average deflection observed was 1.2 mm on the detector. The corresponding transverse momentum gain was 1.5 keV/c, which is $<0.05\%$ of the incident momentum. It should be noted that this value is an underestimate of the effect that the THz pulse has on the electron bunch. The temporal jitter of the instrument caused by slight timing differences between the klystron and the laser reduces $\langle \Delta x_i \rangle$ as the electron bunch is not perfectly phase-locked to the THz pulse. This effect can be seen by measuring the maximum centroid deflection obtained from the streaking patterns shown in figure 3(b). This gives a value of 2 mm, corresponding to a momentum kick of 2.3 keV/c. We note that the details of the interactions between the field and the electron bunch are complicated by the temporal walk off between the THz pulse and the electron bunch, in coupling of the THz fields into the pinhole, and the structure of the local fields especially at the entrance and exit of the pinhole. Such a calculation is beyond the scope of this work and will be the subject of future investigations [37].

These measurements illustrate the use of a pinhole, or any enhancement structure, as a convenient tool of determining both spatial and temporal overlap between the THz pulse and the electron

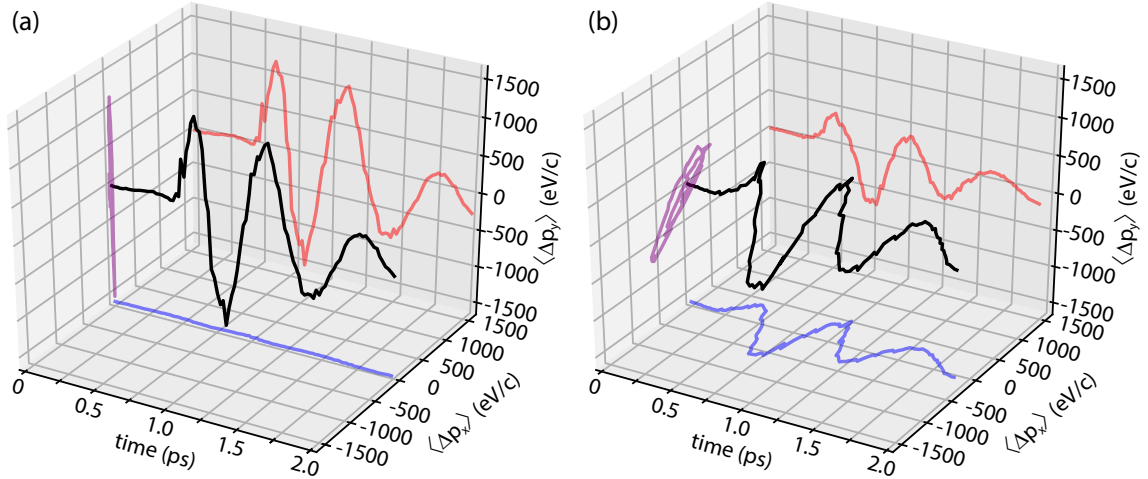


Figure 4. Three dimensional representation of the deflection of the electron bunch by a THz pulse in t, x, y -space. The THz polarization has been set to (a) vertical and (b) $\sim 45^\circ$ by rotating a half-waveplate and the DSTMS crystal.

bunches. At the same time, it is important to note that some commonly used sample preparation tools, such as copper mesh grids, will have the same effect on the entire diffraction pattern. This is not a serious issue in cases where the THz induced response persists long after the main cycle of the THz pulse. In addition, conducting grids can also serve to enhance the THz field near the samples, similar to field enhancement achieved with metamaterials [38, 39].

5 Conclusions and outlook

In conclusion, we have built a new experimental system designed for THz pump MeV-UED probe experiments. This represents the first system suitable for probing with ultrafast electron diffraction the structural dynamics induced by intense THz fields. The two different means of producing THz pulses, using either LN or DSTMS as a nonlinear medium, span a broad frequency range up to 5 THz allowing a broad set of either resonant or non-resonant phenomena to be investigated. The system also retains the ability to excite samples with either intense 800 nm or 400 nm pulses, or to perform double-pump experiments as well. These capabilities enable many classes of experiments to be performed within a short time on the same samples. This is important for accurately elucidating the different responses induced by either THz or optical pumping. We have also demonstrated the capabilities of the instrument by using femtosecond electron bunches to locally characterize the THz field.

The interactions between the THz pulse and the electron beam can be used to characterize the electron bunch in a way that is otherwise inaccessible. Measurement of the THz induced streaking and deflection can be used to as a timing tool for precisely characterizing the temporal jitter of the instrument as well as the duration of the electron bunches. It should also be possible to use this as a means of time-stamping, which would improve the temporal resolution of performed measurements. This instrument also has applications in studies of materials where THz excitation is preferable because energy is more directly transferred to the lattice or other low-energy degrees of freedom. Such measurements will be useful for distinguishing the contributions of electronic and lattice excitations to signals observed in optical pump-probe measurements.

Acknowledgments

The authors thank SLAC management for technical support. This work was supported in part by the U.S. Department of Energy (DOE) Basic Energy Sciences Scientific User Facilities Division Accelerator & Detector R&D program under Contract No. DE-AC02-76SF00515, and the SLAC UED/UEM Initiative Program Development Fund. B.K.O and S.H.G. acknowledge support from the DOE Office of Science, Fusion Energy Science under FWP 100182 M.C.H. is supported by the U.S. Department of Energy, Office of Science, Office of Basic Energy Sciences, under Award No. 2015-SLAC-100238-Funding. AML acknowledges support by the Department of Energy, Office of Science, Basic Energy Sciences, Materials Sciences and Engineering Division, under Contract DE-AC02-76SF00515.

References

- [1] R. J. D. Miller, *Science* **343**, 1108 (2014).

- [2] L. B. Fletcher, H. J. Lee, T. Döppner, E. Galtier, B. Nagler, P. Heimann, C. Fortmann, S. LePape, T. Ma, M. Millot, A. Pak, D. Turnbull, D. A. Chapman, D. O. Gericke, J. Vorberger, T. White, G. Gregori, M. Wei, B. Barbreil, R. W. Falcone, C.-C. Kao, H. Nuhn, J. Welch, U. Zastra, P. Neumayer, J. B. Hastings, and S. H. Glenzer, *Nat. Photonics* **9**, 274 (2015).
- [3] M. Z. Mo, X. Shen, Z. Chen, R. K. Li, M. Dunning, Q. Zheng, S. P. Weathersby, A. H. Reid, R. Co, I. Makasyuk, S. Edstrom, D. McCormick, K. Jobe, C. Hast, S. H. Glenzer, and X. Wang, *Rev. Sci. Instrum.* **87**, 11D810 (2016).
- [4] P. Emma, R. Akre, J. Arthur, R. Bionta, C. Bostedt, J. Bozek, A. Brachmann, P. Bucksbaum, R. Coffee, F. J. Decker, Y. Ding, D. Dowell, S. Edstrom, A. Fisher, J. Frisch, S. Gilevich, J. Hastings, G. Hays, P. Hering, Z. Huang, R. Iverson, H. Loos, M. Messerschmidt, A. Miahnahri, S. Moeller, H. D. Nuhn, G. Pile, D. Ratner, J. Rzepiela, D. Schultz, T. Smith, P. Stefan, H. Tompkins, J. Turner, J. Welch, W. White, J. Wu, G. Yocky, and J. Galayda, *Nat. Photonics* **4**, 641 (2010).
- [5] T. Ishikawa, H. Aoyagi, T. Asaka, Y. Asano, N. Azumi, T. Bizen, H. Ego, K. Fukami, T. Fukui, Y. Furukawa, S. Goto, H. Hanaki, T. Hara, T. Hasegawa, T. Hatsui, A. Higashiya, T. Hirono, N. Hosoda, M. Ishii, T. Inagaki, Y. Inubushi, T. Itoga, Y. Joti, M. Kago, T. Kameshima, H. Kimura, Y. Kirihara, A. Kiyomichi, T. Kobayashi, C. Kondo, T. Kudo, H. Maesaka, X. M. Maréchal, T. Masuda, S. Matsubara, T. Matsumoto, T. Matsushita, S. Matsui, M. Nagasono, N. Nariyama, H. Ohashi, T. Ohata, T. Ohshima, S. Ono, Y. Otake, C. Saji, T. Sakurai, T. Sato, K. Sawada, T. Seike, K. Shirasawa, T. Sugimoto, S. Suzuki, S. Takahashi, H. Takebe, K. Takeshita, K. Tamasaku, H. Tanaka, R. Tanaka, T. Tanaka, T. Togashi, K. Togawa, A. Tokuhisa, H. Tomizawa, K. Tono, S. Wu, M. Yabashi, M. Yamaga, A. Yamashita, K. Yanagida, C. Zhang, T. Shintake, H. Kitamura, and N. Kumagai, *Nat. Photonics* **6**, 540 (2012).
- [6] A. H. Zewail, *Annu. Rev. Phys. Chem.* **57**, 65 (2006).
- [7] R. D. Miller, *Annu. Rev. Phys. Chem.* **65**, 583 (2014).
- [8] E. M. Mannebach, R. Li, K.-A. Duerloo, C. Nyby, P. Zalden, T. Vecchione, F. Ernst, A. H. Reid, T. Chase, X. Shen, S. Weathersby, C. Hast, R. Hettel, R. Coffee, N. Hartmann, A. R. Fry, Y. Yu, L. Cao, T. F. Heinz, E. J. Reed, H. A. Dürr, X. Wang, and A. M. Lindenberg, *Nano Lett.* **15**, 6889 (2015).
- [9] R. Henderson, *Q. Rev. Biophys.* **28**, 171 (1995) .
- [10] J. B. Hastings, F. M. Rudakov, D. H. Dowell, J. F. Schmerge, J. D. Cardoza, J. M. Castro, S. M. Gierman, H. Loos, and P. M. Weber, *Appl. Phys. Lett.* **89**, 184109 (2006).
- [11] X. Shen, R. K. Li, U. Lundström, T. J. Lane, A. H. Reid, S. P. Weathersby, and X. J. Wang, *Ultramicroscopy* **184**, 172 (2018).
- [12] K. Tanaka, H. Hirori, and M. Nagai, *IEEE Trans. Terahertz Sci. Technol.* **1**, 301 (2011).
- [13] M. C. Hoffmann, in *Terahertz Spectrosc. Imaging*, Springer Series in Optical Sciences, Vol. 171, edited by K.-E. Peiponen, A. Zeitler, and M. Kuwata-Gonokami (Springer Berlin Heidelberg, Berlin, Heidelberg, 2013) Chap. 14, pp. 355–388.
- [14] T. Kampfrath, K. Tanaka, and K. A. Nelson, *Nat. Photonics* **7**, 680 (2013).
- [15] H. Y. Hwang, S. Fleischer, N. C. Brandt, B. G. Perkins, M. Liu, K. Fan, A. J. Sternbach, X. Zhang, R. D. Averitt, and K. A. Nelson, *J. Mod. Opt.* **62**, 1447 (2014).
- [16] E. A. Nanni, W. R. Huang, K.-H. Hong, K. Ravi, A. Fallahi, G. Moriena, R. J. Dwayne Miller, and F. X. Kärtner, *Nat. Commun.* **6**, 8486 (2015).

- [17] W. R. Huang, A. Fallahi, X. Wu, H. Cankaya, A.-L. Calendron, K. Ravi, D. Zhang, E. A. Nanni, K.-H. Hong, and F. X. Kärtner, *Optica* **3**, 1209 (2016).
- [18] U. Fröhling, M. Wieland, M. Gensch, T. Gebert, B. Schütte, M. Krikunova, R. Kalms, F. Budzyn, O. Grimm, J. Rossbach, E. Plönjes, and M. Drescher, *Nat. Photonics* **3**, 523 (2009).
- [19] I. Gorgisyan, R. Ischebeck, C. Erny, A. Dax, L. Patthey, C. Pradervand, L. Sala, C. Milne, H. T. Lemke, C. P. Hauri, T. Katayama, S. Owada, M. Yabashi, T. Togashi, R. Abela, L. Rivkin, and P. Juranić, *Opt. Express* **25**, 2080 (2017).
- [20] R. Ivanov, J. Liu, G. Brenner, M. Brachmanski, and S. Düsterer, *J. Synchrotron Radiat.* **25**, 26 (2018).
- [21] M. C. Hoffmann, I. Grguraš, C. Behrens, C. Bostedt, J. Bozek, H. Bromberger, R. Coffee, J. T. Costello, L. F. DiMauro, Y. Ding, G. Doumy, W. Helml, M. Ilchen, R. Kienberger, S. Lee, A. R. Maier, T. Mazza, M. Meyer, M. Messerschmidt, S. Schorb, W. Schweinberger, K. Zhang, and A. L. Cavalieri, *New J. Phys.* **20**, 033008 (2018).
- [22] C. Kealhofer, W. Schneider, D. Ehberger, A. Ryabov, F. Krausz, and P. Baum, *Science* **352**, 429 (2016).
- [23] R. Kanya and K. Yamanouchi, *Phys. Rev. A* **95**, 1 (2017).
- [24] S. P. Weathersby, G. Brown, M. Centurion, T. F. Chase, R. Coffee, J. Corbett, J. P. Eichner, J. C. Frisch, A. R. Fry, M. Gühr, N. Hartmann, C. Hast, R. Hettel, R. K. Jobe, E. N. Jongewaard, J. R. Lewandowski, R. K. Li, A. M. Lindenberg, I. Makasyuk, J. E. May, D. McCormick, M. N. Nguyen, A. H. Reid, X. Shen, K. Sokolowski-Tinten, T. Vecchione, S. L. Vetter, J. Wu, J. Yang, H. A. Dürr, and X. J. Wang, *Rev. Sci. Instrum.* **86**, 073702 (2015).
- [25] J. Hebling, G. Almási, I. Kozma, and J. Kuhl, *Opt. Express* **10**, 1161 (2002).
- [26] A. G. Stepanov, J. Hebling, and J. Kuhl, *Appl. Phys. Lett.* **83**, 3000 (2003).
- [27] A. G. Stepanov, J. Hebling, and J. Kuhl, *Appl. Phys. B* **81**, 23 (2005).
- [28] K.-L. Yeh, M. C. Hoffmann, J. Hebling, and K. A. Nelson, *Appl. Phys. Lett.* **90**, 171121 (2007).
- [29] A. G. Stepanov, L. Bonacina, S. V. Chekalin, and J.-P. Wolf, *Opt. Lett.* **33**, 2497 (2008).
- [30] C. Vicario, A. V. Ovchinnikov, S. I. Ashitkov, M. B. Agranat, V. E. Fortov, and C. P. Hauri, *Opt. Lett.* **39**, 6632 (2014).
- [31] C. Vicario, B. Monoszlai, and C. P. Hauri, *Phys. Rev. Lett.* **112**, 213901 (2014).
- [32] Z. Bor and B. Rácz, *Opt. Commun.* **54**, 165 (1985).
- [33] J. Hebling, *Opt. Quantum Electron.* **28**, 1759 (1996).
- [34] H. Hirori, A. Doi, F. Blanchard, and K. Tanaka, *Appl. Phys. Lett.* **98**, 091106 (2011).
- [35] Q. H. Park, *Contemp. Phys.* **50**, 407 (2009).
- [36] J. H. Kang and Q. H. Park, *IEEE Trans. Terahertz Sci. Technol.* **6**, 371 (2016).
- [37] R. K. Li, M. C. Hoffmann, E. A. Nanni, S. H. Glenzer, A. M. Lindenberg, B. K. Ofori-Okai, A. H. Reid, X. Shen, S. P. Weathersby, J. Yang, M. Zajac, and X. J. Wang, 1, [arXiv:1805.01979](https://arxiv.org/abs/1805.01979) (2018).
- [38] K. Fan, H. Y. Hwang, M. Liu, A. C. Strikwerda, A. J. Sternbach, J. Zhang, X. Zhao, X. Zhang, K. A. Nelson, and R. D. Averitt, *Phys. Rev. Lett.* **110**, 217404 (2013).
- [39] N. K. Grady, B. G. Perkins, H. Y. Hwang, N. C. Brandt, D. Torchinsky, R. Singh, L. Yan, D. Trugman, S. A. Trugman, Q. X. Jia, A. J. Taylor, K. A. Nelson, and H.-T. Chen, *New J. Phys.* **15**, 105016 (2013).